ACS APPLIED MATERIALS & INTERFACES

Research Article

Cite This: ACS Appl. Mater. Interfaces 2017, 9, 43315−43324

www.acsami.org

Transport Across Heterointerfaces of Amorphous Niobium Oxide and Crystallographically Oriented Epitaxial Germanium

Mantu K. Hudait,*[,†] Michael Clavel,[†] Jheng-Sin Liu,[†] Aheli Ghosh,[†] Nikhil Jain,[†] and Robert J. Bodnar[‡]

[†]Advanced Devices & Sustainable Energy Laboratory (ADSEL), Bradley Department of Electrical and Computer Engineering and [‡]Fluids Research Laboratory, Department of Geosciences, Virginia Tech, Blacksburg, Virginia 24061, United States

ABSTRACT: Because of the high carrier mobility of germanium (Ge) and high dielectric permittivity of amorphous niobium pentoxide (a-Nb_2O_5), Ge/a-Nb_2O_5 heterostructures offer several advantages for the rapidly developing field of oxide-semiconductor-based multifunctional devices. To this end, we investigate the growth, structural, band alignment, and metal−insulator−semiconductor (MIS) electrical properties of physical vapor-deposited Nb_2O_5 on crystallographically oriented (100), (110), and (111)Ge epilayers. The as-deposited Nb_2O_5 dielectrics were found to be in the amorphous state, demonstrating an abrupt oxide/semiconductor heterointerface with respect to Ge, when examined via low- and high-magnification cross-sectional transmission electron microscopy. Additionally, variable-angle spectroscopic ellipsometry and X-ray photoelectron spectroscopy (XPS) were used to independently determine the a-Nb_2O_5 band gap, yielding a direct gap value of 4.30 eV. Moreover, analysis of the heterointerfacial energy band alignment between a-Nb_2O_5 and epitaxial Ge revealed valance band offsets (ΔE_V) greater than 2.5 eV, following the relation $\Delta E_V^{(111)} > \Delta E_V^{(110)} > \Delta E_V^{(100)}$. Similarly, utilizing the empirically determined a-Nb_2O_5 band gap, conduction band offsets (ΔE_C) greater than 0.75 eV were found, likewise following the relation $\Delta E_C^{(110)} > \Delta E_C^{(100)} > \Delta E_C^{(111)}$. Leveraging the reduced ΔE_C observed at the a-Nb_2O_5/Ge heterointerface, we also perform the first experimental investigation into Schottky barrier height reduction on n-Ge using a 2 nm a-Nb_2O_5 interlayer, resulting in a 20× increase in reverse-bias current density and improved Ohmic behavior.

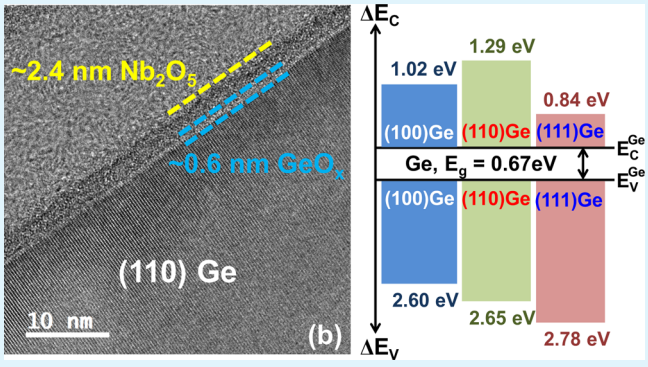

KEYWORDS: *germanium, niobium oxide, band offset, X-ray photoelectron spectroscopy, metal−insulator−semiconductor*

INTRODUCTION

Niobium oxide thin films have been the focus of several decades of research due to their application in composite high-κ gate dielectrics,[1−3] resistive memory devices,[4−6] gas- and biochemical-sensors,[7−11] transparent conducting oxides,[12] dye-sensitized solar cells,[13,14] photodiodes and batteries,[11−18] photochromatic coatings,[19−25] and as insulators in thin-film transistors,[26] metal−insulator transistor-based devices,[26] and metal−insulator−metal capacitors.[5] Among all transition metal oxides, niobium pentoxide (Nb_2O_5) in particular has the highest relative dielectric permittivity (>30) in its amorphous state,[1,12,28] which also exhibits electrochromic behavior.[14] Additionally, several research efforts[14,22,24,29,30] have demonstrated the effect of divergent oxide stoichiometry on niobium oxide conductivity, linking the complexity in polymorph variety (i.e., cubic NbO, tetragonal, rutile, or monoclinic NbO_2, and orthorhombic, monoclinic, tetragonal, or psuedohexagonal Nb_2O_5) and oxide crystallinity with macroscopic material characteristics.[12] Explicitly, the dominant niobium oxide polymorph has been shown to contribute toward conducting (NbO), semiconducting (NbO_2), or insulating (Nb_2O_5) behavior.[31,32] Because of its insulating nature, Nb_2O_5 has been proposed as part of a composite high-κ gate dielectric for p-type silicon (Si) metal−oxide−semiconductor capacitors;[1] however, the large oxide-trapped charge density observed in such films resulted in highly hysteretic behavior.[32−34] Despite the large number of investigations and wide range of applications discussed in the literature, no report exists pertaining to the structural, chemical, or electrical properties of niobium oxide thin films integrated on epitaxial Ge layers. This could be due to the difficulties in controlling niobium oxide polymorphism[12] or disorder induced at the oxide/semiconductor interface as a result of the sample preparation technique employed, that is, laser ablation or sputtering,[1,28,35−40] atomic layer deposition,[33,34,41] chemical vapor deposition (CVD),[2,24,27,42,43] sol−gel processing,[19] or thermal evaporation.[44−47] It has been reported[33] that CVD Nb_2O_5 films remain amorphous below 400 °C, irrespective of substrate material, except when deposited on polycrystalline indium−tin oxide (ITO). During such depositions, Nb_2O_5 was found to

Received: May 10, 2017
Accepted: November 16, 2017
Published: November 16, 2017

DOI: 10.1021/acsami.7b06601
ACS Appl. Mater. Interfaces 2017, 9, 43315−43324

crystallize when deposited at 265−275 °C, thus indicating that substrate surface chemistry plays a key role in altering the microstructural and macroscopic properties of Nb_2O_5 materials.

In this article, we demonstrate the microstructural, electronic band structure, and heterointerfacial chemical properties of physical vapor deposited (PVD) amorphous Nb_2O_5 (a-Nb_2O_5) on epitaxial, unintentionally-doped n-type (100)Ge, (110)Ge, and (111)Ge. Raman spectroscopy and cross-sectional transmission electron microscopy (TEM) were used to verify the amorphous nature of the as-deposited Nb_2O_5 as well as to investigate the long- and short-range order uniformity of the Nb_2O_5/Ge heterointerface. X-ray photoelectron spectroscopy (XPS) was utilized in the determination of the heterointerface energy band discontinuities at the a-Nb_2O_5/Ge interface. Lastly, the electrical properties of a-Nb_2O_5/(100)Ge metal−insulator−semiconductor (MIS) devices were evaluated under three process conditions: (i) as-fabricated (i.e., unannealed) and annealed at (ii) 250 °C and (iii) 350 °C in a forming gas (5% H_2/95% N_2) ambient. Additional details regarding the deposition conditions of the Nb_2O_5 films are shown in Table I.

Table I. Process Parameters Employed during the Deposition of the Nb_2O_5 Layers Using Physical Vapor Deposition (PVD)[a]

PVD process parameter	value
chamber base pressure	~10^{-6} Torr
oxygen (ultrahigh purity (UHP)) flow rate	5 sccm
substrate temperature	27 °C
substrate rotational speed	5 rpm
substrate−target separation	57 cm
nominal Nb_2O_5 deposition rate	~0.2 Å/s
nominal Nb_2O_5 thickness	2−5 nm

[a]All depositions were performed at room temperature.

RESULTS AND DISCUSSION

Material Characterization. *Raman Spectroscopic Analysis.* The Raman spectrum of niobium oxide has been studied intensely by several researchers,[28,48,49] including its temperature dependence from room temperature to 300 °C as well as the effect of quenching from 1200 °C on the crystallinity of powdered Nb_2O_5. In the present work, the Raman spectra of nominally 5 nm PVD Nb_2O_5 films deposited on crystallographically oriented epitaxial Ge as well as on (100)Si have been compared, as shown in Figure 1. Because of the saturation of the detector during spectral acquisition (30 s cumulative scan time), a short duration acquisition (5 s cumulative scan time) was utilized in locating the first-order Si Raman mode at 520.56 cm^{-1} (Figure 1 inset). Similarly, the first-order Ge Raman mode was observed at 300 cm^{-1}. The observed Raman signal in the wavenumber range of 900−1000 cm^{-1} was due to multiphonon second-order Raman scattering corresponding to three, doubly degenerate transverse optical phonon modes at the X, W, and L valleys in crystalline bulk silicon.[50,51] The expected Raman scattering due to crystalline or polycrystalline Nb_2O_5 phonon modes was not observed, thereby confirming the amorphous nature of the as-deposited Nb_2O_5 films. Moreover, no dependence on substrate orientation or type was observed in the recorded Raman spectra. Thus, for PVD Nb_2O_5 deposited at room temperature on epitaxial Ge or (100)Si, the current observation of amorphous oxide deposition is consistent with previously reported data.[1,28,43]

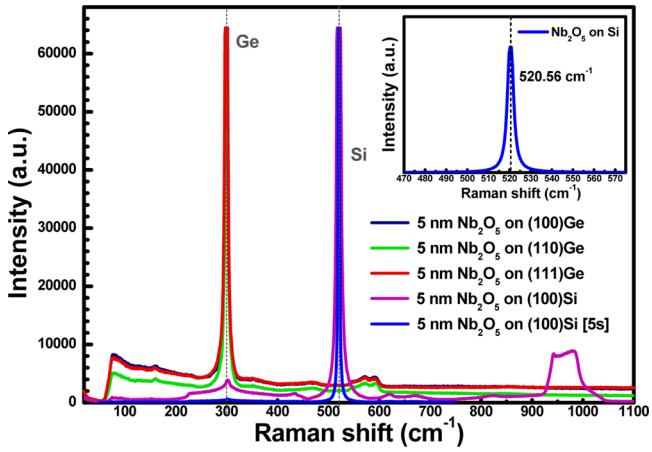

Figure 1. Raman spectra of the as-deposited Nb_2O_5 films on (100)Ge, (110)Ge, (111)Ge, and (100)Si recorded using a cumulative scan time of 30 s. Inset shows the first-order Si Raman mode at 520.56 cm^{-1} for a scan time of 5 s.

TEM Analysis. Low- and high-magnification cross-sectional TEM micrographs of the Nb_2O_5/Ge/(100)GaAs, Nb_2O_5/Ge/(110)GaAs, and Nb_2O_5/Ge/(111)GaAs heterostructures are shown in Figure 2a−c and d−f respectively. One can find from Figure 2a−c that the Nb_2O_5 deposition exhibited long-range relative uniformity across the Nb_2O_5/Ge heterointerface independent of Ge surface orientation. This is further reinforced via the short-range abruptness at the Nb_2O_5/Ge interface observed in the high-magnification TEM micrographs in Figure 2d−f. One can also find from Figure 2d−f that an ultrathin (≤0.6 nm, contingent on surface orientation) GeO_x interfacial layer was unintentionally formed during the Nb_2O_5 deposition. The formation of such an interfacial layer could occur due to the preferential bonding of oxygen with Ge prior to and at the initial stages of the Nb_2O_5 deposition or might arise from an O scavenging or Ge migration process through the Nb_2O_5 film. The effect of oxide deposition in an O_2 ambient will be elucidated via X-ray photoelectron spectroscopy (XPS) analysis in a latter section, which will shed further light on the nature of the chemical bonding at the Nb_2O_5/Ge interface and be used to identify whether substantial diffusion of atomic species across the interface has occurred.

Spectroscopic Ellipsometry Analysis. A wide range of band gap values for Nb_2O_5 have been reported in the literature, ranging from 3.35 to 5.3 eV.[12,23,25,44] Thus, a precise determination of the band gap of the as-deposition a-Nb_2O_5 thin films will be essential in determining the conduction band offset at the Nb_2O_5/Ge heterointerface and accordingly the applicability of the Nb_2O_5/Ge heterojunction to novel oxide/semiconductor functionality. To this end, wavelength and incidence angle-dependent ellipsometry data was used to model the thickness and optical parameters (refractive index, n, and extinction coefficient, k) of the as-deposited Nb_2O_5/(100)Ge heterostructure. Figure 3a,b shows the wavelength-dependent absorption coefficient (α) and Tauc plot of the modeled Nb_2O_5 optical response, respectively. The absorption coefficient, α, can be expressed in terms of the (direct) optical band gap energy, E_g, as $(\alpha h\nu)^2 = A(h\nu - E_g)$, where A is a constant and $h\nu$ is the incident photon energy. By extrapolation of the linear emission regime to the baseline emission, one can utilize the Tauc plot to accurately estimate the optical band gap of a thin film. For a fitted thickness of 4.12 nm (nominally 5 nm as targeted during

DOI: 10.1021/acsami.7b06601
ACS Appl. Mater. Interfaces 2017, 9, 43315−43324

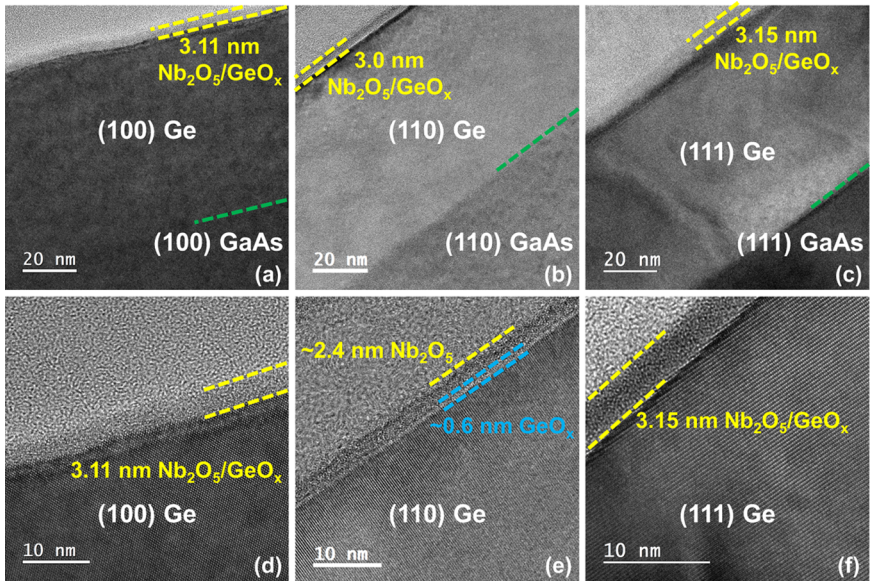

Figure 2. (a–c) Low-magnification cross-sectional TEM (X-TEM) micrographs of the Nb_2O_5/Ge/(100)GaAs, Nb_2O_5/Ge(110)GaAs, and N_2O_5/Ge/(111)GaAs heterostructures, respectively. (d–f) High-magnification X-TEM micrographs of the Nb_2O_5/(100)Ge, Nb_2O_5/(110)Ge, and Nb_2O_5/(111)Ge heterointerfaces, respectively, revealing the short-range uniformity of the Nb_2O_5/Ge interface as well as the formation of a quantifiable ~0.6 nm thick GeO_x interfacial region during Nb_2O_5 deposition on (110)Ge.

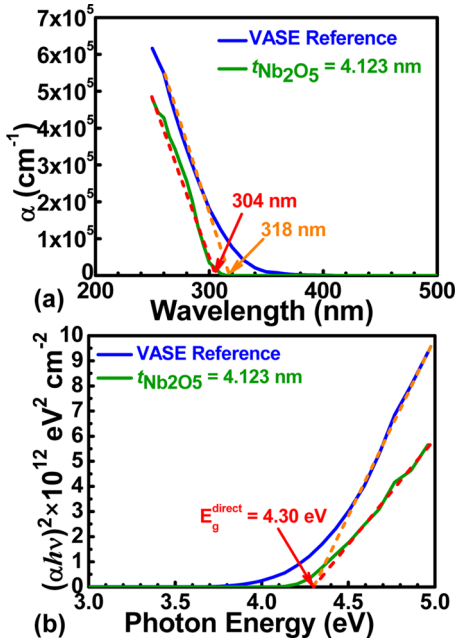

Figure 3. (a) Experimental absorption coefficient as a function of wavelength for a model Nb_2O_5 thickness of 4.12 nm, as determined by variable-angle spectroscopic ellipsometry (VASE). (b) Tauc plot of the fitted Nb_2O_5 optical data indicating a direct band gap energy of 4.3 eV. Reference Nb_2O_5 optical data included for comparison.

PVD), a band gap value of 4.3 eV was found for the Nb_2O_5 layer on (100)Ge. Also included in Figure 3a,b is reference amorphous Nb_2O_5 ellipsometry data provided by the J.A. Woollam company for comparison with the current results. It should be noted that the band gap energy found is more suited toward composite high-κ gate dielectric applications,[52,53] which will therefore require further investigation via determination of the energy band discontinuities at the Nb_2O_5/Ge interface as well as study of the electrical properties of Nb_2O_5/Ge metal–insulator–semiconductor devices.

XPS Analysis: Band Alignment. In this work, X-ray photoelectron spectroscopy (XPS) was used to evaluate the heterojunction band offsets and independently corroborate the Nb_2O_5 band gap value previously determined. This technique combines measurement of core levels (CLs), valence band maxima (VBM), and spectral energy loss peaks to determine the electronic structure at the Nb_2O_5/Ge heterointerface. The recorded XPS spectra provide the energy separations between the relevant material atomic CLs (e.g., Ge 3d) and their respective VBM, as well as the energy separation of material CLs due to band bending at the heterointerface. Using these binding energy (BE) separations, the heterojunction valence band offset (ΔE_V) for Nb_2O_5 on Ge can be determined. Figures 4–6 show the XPS spectra of the (a) Nb 3d CL ($E^{Nb_2O_5}_{Nb\ 3d_{5/2}}$) and VBM ($E^{Nb_2O_5}_{VBM}$) binding energies (BEs) from 5 nm Nb_2O_5 on (100)Ge, (110)Ge, (111)Ge, (b) Ge 3d ($E^{Ge}_{Ge\ 3d_{5/2}}$), and Nb 3d ($E^{Nb_2O_5}_{Nb\ 3d_{5/2}}$) CL BE spectra from the Nb_2O_5/Ge heterointerface on (100)Ge, (110)Ge, (111)Ge, and (c) Ge 3d CL and VBM (E^{Ge}_{VBM}) BEs from bulklike epitaxial (100)Ge, (110)Ge, and (111)Ge surfaces, respectively. The symmetry and BE position of the as-deposited niobium oxide Nb $3d_{5/2}$ and Nb $3d_{3/2}$ spectral features in (a) and (b) indicate the deposition of stoichiometric Nb_2O_5.[28,30] Additionally, the measured O 1s XPS spectra recorded from the bulklike, 5 nm Nb_2O_5 surfaces were used to determine the band gap of Nb_2O_5 as a function of crystallographic orientation. Following the procedures introduced in refs 54–57, a linear fitting of the onset of emission following the O 1s core level (with respect to the background emission in said spectral region) allows for an extraction of the oxide band gap. Such emission can be physically described as the result of inelastic loss experienced by photogenerated electrons excited across the oxide band gap; hence, its applicability in the determination of oxide bandgaps. Correspondingly, the experimentally derived Nb_2O_5 band gap values obtained from fitting of the O 1s loss spectra are tabulated in

DOI: 10.1021/acsami.7b06601
ACS Appl. Mater. Interfaces 2017, 9, 43315–43324

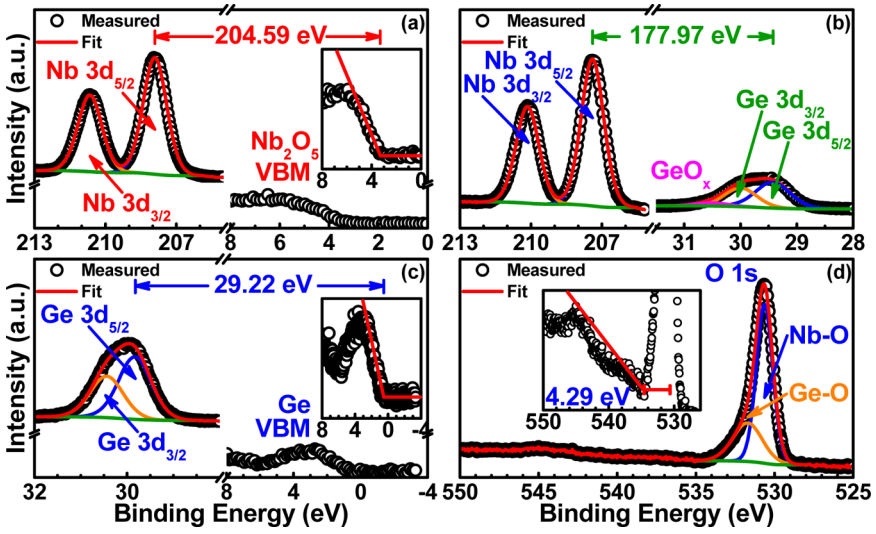

Figure 4. Representative XPS spectra of the (a) Nb 3d ($E^{Nb_2O_5}_{Nb\ 3d_{5/2}}$) core level (CL) and valence band maximum ($E^{Nb_2O_5}_{VBM}$) binding energies (BEs) from 5 nm Nb_2O_5, (b) Nb 3d and Ge 3d ($E^{(100)Ge}_{Ge\ 3d_{5/2}}$) CL BEs from the Nb_2O_5/(100)Ge interface, (c) Ge 3d CL and VBM ($E^{(100)Ge}_{VBM}$) BEs from (100)Ge, and (d) O 1s CL BE and loss spectra from 5 nm Nb_2O_5 on (100)Ge, respectively.

Table II. We note that the Nb_2O_5 band gap on (100)Ge, i.e., 4.3 eV (Figure 4c), is in excellent agreement with the modeled optical band gap determined by variable-angle spectroscopic ellipsometry, providing further confidence in the empirical band gap of PVD Nb_2O_5 used in this work.

Table II. Core Level and Valence Band Maxima Binding Energy Separations and Band Offset Parameters for Nb_2O_5 on Epitaxial (100)Ge, (110)Ge, and (111)Ge

binding energy separation	(100)Ge	(110)Ge	(111)Ge
$E^{Ge}_{Ge\ 3d} - E^{Ge}_{VBM}$	29.22 ± 0.05	29.11 ± 0.05	29.29 ± 0.05
$E^{Nb_2O_5}_{Nb\ 3d_{5/2}} - E^{Nb_2O_5}_{VBM}$	204.59 ± 0.05	204.45 ± 0.05	204.59 ± 0.05
$E^{Nb_2O_5}_{Nb\ 3d_{5/2}} - E^{Ge}_{Ge\ 3d}$	177.97 ± 0.05	177.99 ± 0.05	177.93 ± 0.05
ΔE_V (eV)	2.60 ± 0.05	2.65 ± 0.05	2.78 ± 0.05
$E_G^{Nb_2O_5}$ (eV)	4.29	4.61	4.29
ΔE_C (eV)	1.02 ± 0.1	1.29 ± 0.1	0.84 ± 0.1

Following the methodology introduced by Kraut et al.,[58] the valence band discontinuity at an oxide/semiconductor or semiconductor/semiconductor interface can be expressed as[58−62]

$$\Delta E_V = (E^{Nb_2O_5}_{Nb\ 3d_{5/2}} - E^{Nb_2O_5}_{VBM}) - (E^{Ge}_{Ge\ 3d} - E^{Ge}_{VBM}) - (E^{Nb_2O_5}_{Nb\ 3d_{5/2}} - E^{Ge}_{Ge\ 3d})^i \quad (1)$$

where $(E^{Nb_2O_5}_{Nb\ 3d_{5/2}} - E^{Nb_2O_5}_{VBM})$, $(E^{Ge}_{Ge\ 3d} - E^{Ge}_{VBM})$, and $(E^{Nb_2O_5}_{Nb\ 3d_{5/2}} - E^{Ge}_{Ge\ 3d})^i$ are the binding energy separations corresponding to the bulklike Nb_2O_5, bulklike Ge, and Nb_2O_5/Ge heterointerface. It should be noted that due to the fixed energy separation

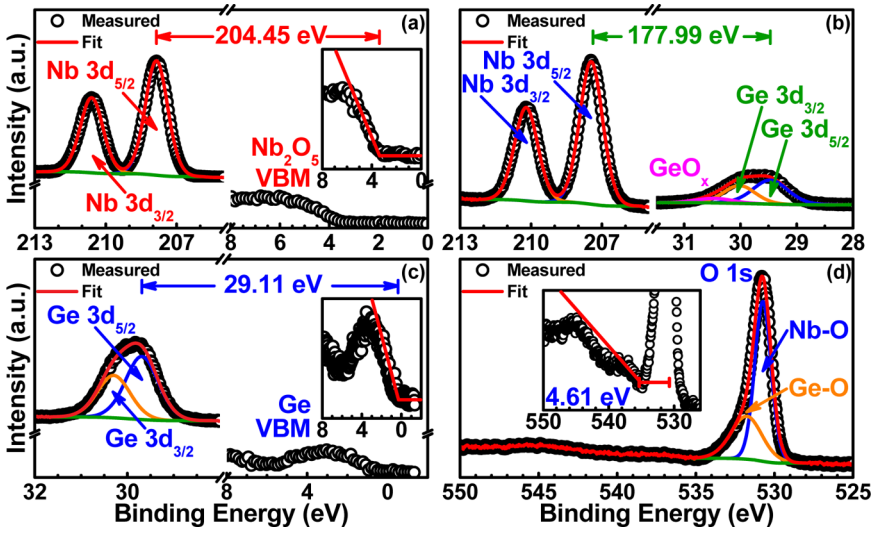

Figure 5. Representative XPS spectra of the (a) Nb 3d ($E^{Nb_2O_5}_{Nb\ 3d_{5/2}}$) core level (CL) and valence band maximum ($E^{Nb_2O_5}_{VBM}$) binding energies (BEs) from 5 nm Nb_2O_5, (b) Nb 3d and Ge 3d ($E^{(110)Ge}_{Ge\ 3d_{5/2}}$) CL BEs from the Nb_2O_5/(110)Ge interface, (c) Ge 3d CL and VBM ($E^{(110)}_{VBM}$) BEs from (110)Ge, and (d) O 1s CL BE and loss spectra from 5 nm Nb_2O_5 on (110)Ge, respectively.

DOI: 10.1021/acsami.7b06601
ACS Appl. Mater. Interfaces 2017, 9, 43315−43324

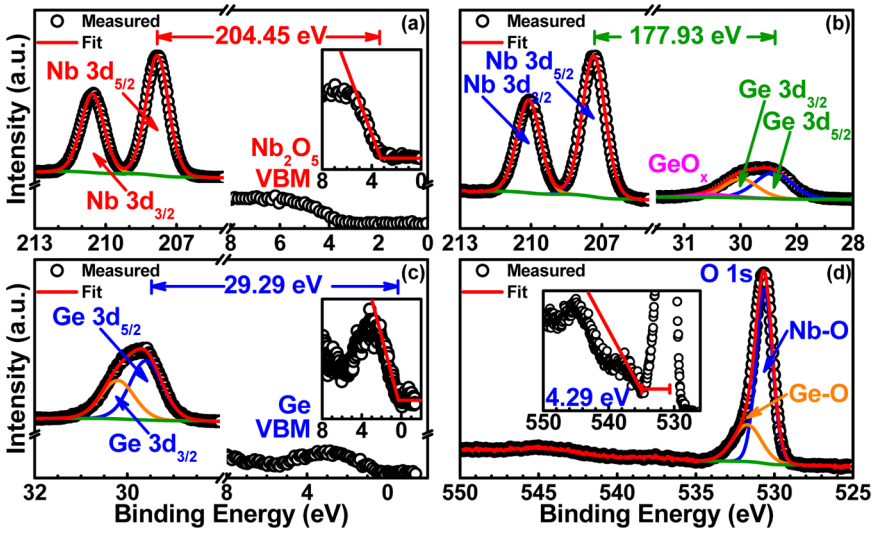

Figure 6. Representative XPS spectra of the (a) Nb 3d ($E_{\mathrm{Nb\ 3d_{5/2}}}^{\mathrm{Nb_2O_5}}$) core level (CL) and valence band maximum ($E_{\mathrm{VBM}}^{\mathrm{Nb_2O_5}}$) binding energies (BEs) from 5 nm Nb_2O_5, (b) Nb 3d and Ge 3d ($E_{\mathrm{Ge\ 3d_{5/2}}}^{(111)\mathrm{Ge}}$) CL BEs from the Nb_2O_5/(111)Ge interface, (c) Ge 3d CL and VBM ($E_{\mathrm{VBM}}^{(111)}$) BEs from (111)Ge, and (d) O 1s CL BE and loss spectra from 5 nm Nb_2O_5 on (111)Ge, respectively.

between the spin−orbit coupled Nb 3d or Ge 3d CLs, the measured ΔE_V does not depend on selection of either the $3d_{5/2}$ or $3d_{3/2}$ spectral feature. The binding energy separations between the bulklike Nb_2O_5 Nb 3d CL and VBM are shown in Figures 4a, 5a, and 6a, for the (100), (110), and (111) orientations, respectively. Likewise, the heterointerfacial degree of band bending, i.e., the binding energy separation between Nb 3d and Ge 3d CLs at the Nb_2O_5/Ge heterointerface, are shown in Figures 4b, 5b, and 6b. Similarly, the binding energy separations between the bulklike epitaxial Ge 3d CL and VBM are shown in Figures 4c, 5c, and 6c. Utilizing these data and eq 1, the corresponding experimental ΔE_V at the (100), (110), and (111) Nb_2O_5/Ge junctions were 2.60 ± 0.05, 2.65 ± 0.05, and 2.78 ± 0.05 eV respectively. Finally, the conduction band offset (ΔE_C) for each Nb_2O_5/Ge heterointerface can be calculated from the measured ΔE_V and known material bandgaps, i.e.,

$$\Delta E_C = E_g^{\mathrm{Nb_2O_5}} - E_g^{\mathrm{Ge}} + \Delta E_V \quad (2)$$

where $E_g^{\mathrm{Nb_2O_5}}$ is the experimental Nb_2O_5 band gap and E_g^{Ge} is the literature-reported band gap value for Ge (i.e., 0.67 eV). Using eq 2, the calculated ΔE_C for the (100), (110), and (111) Nb_2O_5/Ge heterojunctions were 1.02 ± 0.1, 1.29 ± 0.1, and 0.84 ± 0.1 eV, respectively. For clarity, the aforementioned results have been summarized in Table II.

As can be seen from Table II, the measured ΔE_V values were above 2.5 eV, irrespective of crystallographic orientation, following the relation $\Delta E_V^{(111)} > \Delta E_V^{(110)} > \Delta E_V^{(100)}$. Similarly, ΔE_C values greater than 0.75 eV were calculated, likewise obeying the relation $\Delta E_C^{(110)} > \Delta E_C^{(100)} > \Delta E_C^{(111)}$. The influence of crystallographic orientation on the experimental band discontinuities is posited to be the result of: (i) differences in Nb_2O_5 film quality; (ii) Ge surface reconstruction; and (iii) the charge neutrality level at each heterointerface, all of which are expected to vary as a function of surface orientation.[59,60] Several models have been developed, as reported in ref 60, to account for these effects, including the aforementioned surface reconstruction dependence on crystallographic orientation as well as differing bond terminations[60] and surface polarities (i.e., polar vs nonpolar surfaces).[60] Indeed, a previous report[59] has shown that the surface reconstruction of epitaxial Ge is impacted by crystallographic orientation, revealing (2 × 2), (3 × 4), and (1 × 1) reconstruction patterns on (100)Ge, (110)Ge, and (111)Ge epilayers, respectively. Thus, the differences in ΔE_V observed in this work are likely due to the surface orientation impact on surface reconstruction and its subsequent effect on interfacial bonding. Moreover, although an O_2 ambient was used during deposition of the Nb_2O_5 films, the low thermal energy (i.e., solely residual substrate heating during oxide evaporation) of the system would be expected to minimize the formation of a relatively thick GeO_x interfacial layer. As observed in Figure 2d−f, the GeO_x interlayer was observed to reach a maximum thickness of 0.6 nm on (110)Ge, whereas the distinctly reduced GeO_x thickness on (100)Ge and (111)Ge obfuscated precise GeO_x thickness determination. Furthermore, as demonstrated in ref 58, the GeO_x VBM occurs at ∼4 eV, which is approximately 1 eV higher in binding energy than the Nb_2O_5 VBM reported in this work. As a result, minimal convolution of the GeO_x and Nb_2O_5 valence spectra would be expected, indicating that the GeO_x interlayer will have no observable impact on the measured band discontinuities. Figure 7a−c illustrates the schematic band alignments for the (100), (110), and (111) Nb_2O_5/Ge heterostructures, respectively, whereas Figure 8 presents a summary of the band alignment distribution (i.e., ΔE_V vs ΔE_C) as compared between crystallographic orientations. Although these results indicate that GeO_x formation would have little impact on the experimental band alignments studied here, one could expect that the formation of a GeO_x interlayer and its thermodynamic stability (or instability) at the interface would have an observable influence on the electrical and chemical properties of Nb_2O_5/Ge heterostructures. The remaining sections will attempt to elucidate these concepts and evaluate the electrical characteristics of Nb_2O_5-based metal−insulator−semiconductor devices.

XPS Analysis: Nb_2O_5/Ge Intermixing. Figure 9 shows the Nb 4p and Ge 3d binding energy spectra recorded from the surface of 5 nm Nb_2O_5 layers deposited on (a) (100)Ge, (b) (110)Ge, and (c) (111)Ge. Clear evidence of Ge out-diffusion through Nb_2O_5 to the oxide surface was revealed by the presence of

DOI: 10.1021/acsami.7b06601
ACS Appl. Mater. Interfaces 2017, 9, 43315−43324

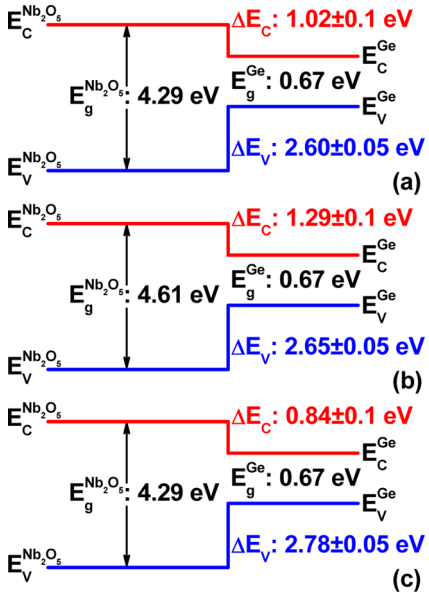

Figure 7. Schematic flat-band energy band alignments for the (a) Nb_2O_5/(100)Ge, (b) Nb_2O_5/(110)Ge, and (c) Nb_2O_5/(111)Ge heterojunctions, as determined via XPS analysis, respectively. The literature-reported Ge band gap value of 0.67 eV was used in this work.

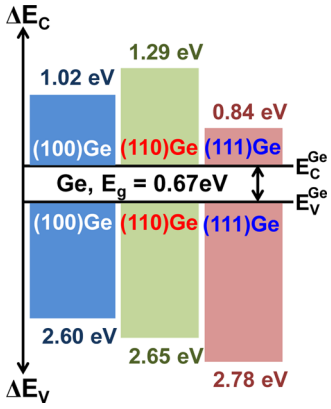

Figure 8. Empirical distribution of the (a) valence band and (b) conduction band offsets for a-Nb_2O_5 on crystallographically oriented (100)Ge, (110)Ge, and (111)Ge epilayers.

GeO_2-related photoemission features between 32 and 33.5 eV. Moreover, the intensity of these features was found to be highest on (110)Ge, indicating increased Ge out-diffusion through the Nb_2O_5/(110)Ge heterostructure. This result mirrors the increased O 1s secondary spectral feature observed in Figure 5c, as compared to that in Figures 4c and 6c, thereby suggesting that the larger Nb_2O_5 band gap on (110)Ge was a result of increased GeO_2 formation and out-diffusion and/or the creation of a complex $(Nb_2O_5)_{1-x}(GeO_2)_x$ composite oxide. Moreover, the symmetry of the Nb 3d, Nb 4p, and Ge 3d spectral features rules out the formation of nonstoichiometric suboxide networks in the as-deposited Nb_2O_5, indicating that the formation and subsequent out-diffusion of GeO_2 was due to the O_2 ambient used during deposition as opposed to the scavenging of interfacial oxygen from Nb_2O_5.

Nb_2O_5/Ge Metal–Insulator–Semiconductor Properties: Role of Nb_2O_5 Interlayer. Several transition metal oxides have been recently proposed for use as an interfacial layer between contact metals and the n-type Ge surface. By inserting

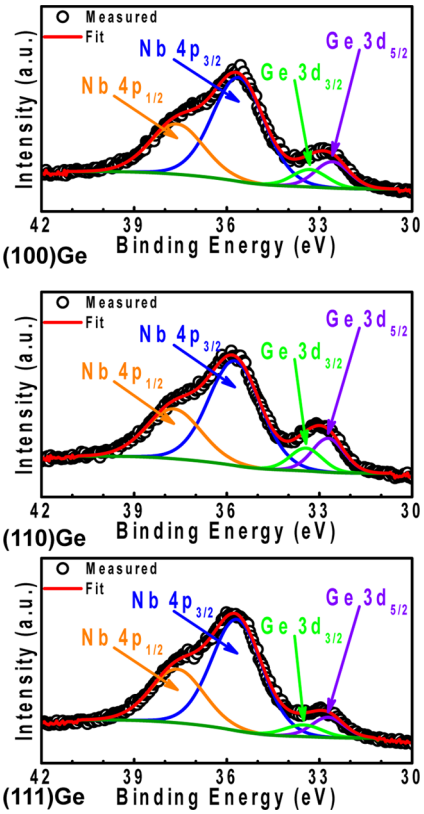

Figure 9. Nb 4p and Ge 3d core level binding energy spectra from 5 nm Nb_2O_5 deposited on (100)Ge, (110)Ge, and (111)Ge epilayers, revealing the formation of GeO_2 and its subsequent out-diffusion through the Nb_2O_5 dielectric.

an ultrathin insulating layer, the evanescent coupling of the metal wavefunction with states in the Ge band gap (i.e., the metal-induced gap states, MIGS) can be reduced or eliminated, thereby minimizing the Schottky barrier at the metal/semiconductor interface and decreasing contact resistance. Recent results have demonstrated that insertion of a heavily-doped interfacial insulating layer with low conduction band offsets can dramatically improve the contact resistance associated with metal/n-Ge contacts.[63,64] To this end, insulators with low or zero conduction band offsets are expected to facilitate Ohmic metal–insulator–semiconductor (MIS) behavior by reducing the insulator tunneling barrier height, thereby enhancing tunneling current. Figure 10a shows the current density versus applied voltage (J–V) characteristics of Au/Ti/Nb_2O_5/n-(100)Ge MIS devices with (□) and without (○) the inclusion of a 2 nm Nb_2O_5 interlayer. The J–V characteristics of the MIS contact utilizing the Nb_2O_5 interlayer showed a ~20× increase in reverse-bias current density as compared to that of the control Au/Ti/n-(100)Ge structure. These results indicate that the Nb_2O_5 insulating layer was effective in reducing MIGS at the Ti/n-(100)Ge interface and sufficiently thin such that direct tunneling current was the predominant current mechanism observed at low bias. The asymmetry in current density between forward and reverse bias is likely due to the large asymmetric distribution in the measured valence and conduction band discontinuities and thus in the forward- and reverse-bias tunneling barrier heights. Figure 10b further elucidates the role of the 2 nm Nb_2O_5 interlayer in reducing the Schottky barrier of the MIS contact to n-(100)Ge by highlighting the complete empirical band

DOI: 10.1021/acsami.7b06601
ACS Appl. Mater. Interfaces 2017, 9, 43315–43324

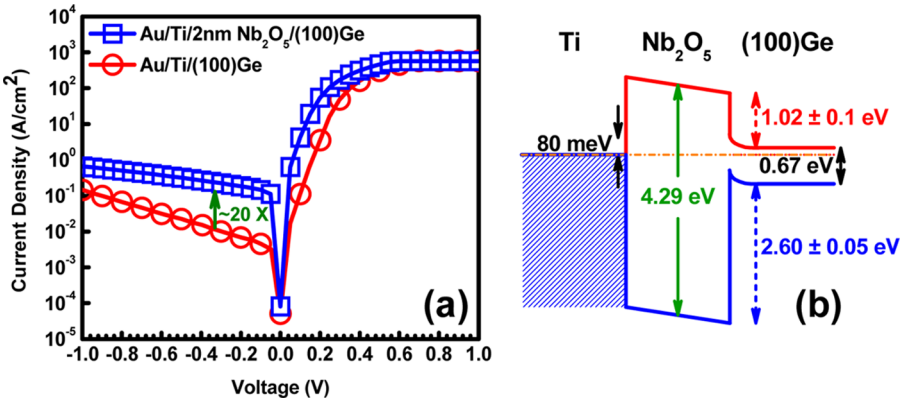

Figure 10. (a) Current density vs applied voltage characteristics for contacts to (100)n-Ge (6×10^{16} cm^{-3}) with (□) and without (○) an Nb_2O_5 interlayer. (b) Experimental Au/Ti/Nb_2O_5/(100)Ge electronic band structure, as determined via XPS.

Table III. Comparison of Previously Reported Data for MIS Contacts to n-(100)Ge with the Findings Reported Herein[a]

insulator	insulator thickness (nm)	insulator band gap (eV)	ΔE_C (eV)	ΔE_V (eV)	Ge doping (cm^{-3})	Φ_b (meV)	current density increase, J_{off} ($V = -0.1$ V)	ref
Ti/n-Ge					1×10^{17}	550		63
Al_2O_3	1	6.06	1.7	3.7	$\sim 10^{19}$		negligible	64
TiO_2	8.8	3.5	−0.06	2.9	$\sim 10^{19}$	65	1200×	64
ITO	4.8	3.6	−0.19	3.13	1×10^{17}		1000×	63
n^+-ZnO/Al	0.7	3.25	−0.14	2.73	1×10^{17}		700×	63
Nb_2O_5	2	4.29	1.02	2.60	6×10^{16}	80	20×	this study

[a]Only data for optimal insulator thicknesses have been tabulated.

diagram of the Au/Ti/Nb_2O_5/n-(100)Ge structure, as determined via XPS. Utilizing the modified Kraut methodology for a metal/semiconductor (oxide) heterostructure, the Schottky barrier height at the metal/semiconductor (oxide) heterointerface can be expressed as[58]

$$\Phi_b = (E_{Ge\ 3d_{5/2}}^{(100)Ge} - E_{VBM}^{(100)Ge})^{bulk} + E_g^{Ge} - (E_{Ge\ 3d_{5/2}}^{(100)Ge})^{i} \quad (3)$$

where $(E_{Ge\ 3d_{5/2}}^{(100)Ge} - E_{VBM}^{(100)Ge})^{bulk}$ is the Ge 3d CL and VBM BE separation taken from the bulklike epitaxial (100)Ge surface, E_g^{Ge} is the Ge band gap (0.67 eV), and $(E_{Ge\ 3d_{5/2}}^{(100)Ge})^{i}$ is the Ge 3d CL measured at the metal/semiconductor interface. Using the aforementioned bulklike epitaxial (100)Ge 3d CL and VBM BE separation of 29.22 eV in conjunction with the measured Ge $3d_{5/2}$ CL BE of 29.81 eV recorded from the Au/Ti/Nb_2O_5/n-(100)Ge MIS heterointerface, Φ_b was determined to be ∼80 meV. Table III compares these results with previously reported MIS contact data to n-(100)Ge. As can be seen from Table III, although increased substrate doping can be expected to facilitate Ohmic contact behavior, the contact resistance in Nb_2O_5-based MIS devices is chiefly dominated by increased tunneling resistance due to the ∼1.0 eV conduction band offset.

Nb_2O_5/Ge Metal−Insulator−Semiconductor Properties: Role of Annealing. During high-volume semiconductor manufacturing, high-temperature annealing is often used to recrystallize implant-damaged surfaces, activate dopants, or sinter metal/semiconductor contact alloys. Thus, understanding the impact of annealing on the MIS properties of Nb_2O_5-based MIS devices is necessary to examine more thoroughly the scope of the applicability of such devices. To this end, Au/Ti/Nb_2O_5/n-(100)Ge MIS devices were annealed in a forming gas ambient at 250 and 350 °C for 4 min. Figure 11 shows the $J-V$ characteristics of the as-fabricated (unannealed) devices (□) and those annealed at 250 °C (◇) and 350 °C (△). One can

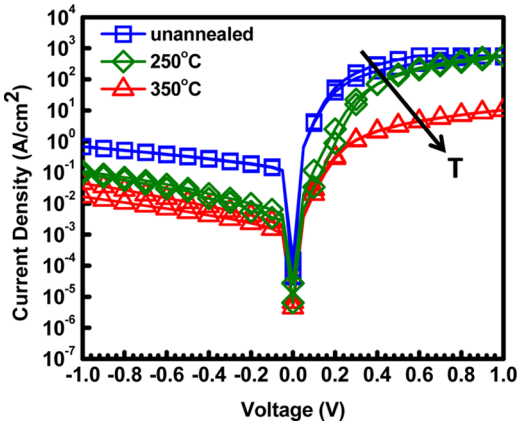

Figure 11. Current density vs voltage characteristics for MIS contacts to (100) n-Ge (6×10^{16} cm^{-3}) prior to annealing (□) and when annealed at 250 °C (◇) and 350 °C (△).

find from Figure 11 that both reverse and forward bias current densities exhibited a dramatic reduction as a function of increasing thermal budget. This was attributed to the reduction of both oxide (i.e., O vacancy) and interfacial (i.e., uncoordinated Ge atoms) defects during annealing, resulting in less electrically active defect states that could contribute to conduction trap-assisted tunneling. Correspondingly, these results indicate that thermal budget is a key parameter when integrating Nb_2O_5 insulating layers on Ge and must be reduced to maximize tunneling current density in ultrathin Nb_2O_5/Ge-based heterojunctions. Moreover, these findings also suggest that use of nonstoichiometry niobium oxides may enhance NbO_x/Ge MIS contact performance via increased trap-assisted tunneling and therefore show enhanced low-bias current density.

DOI: 10.1021/acsami.7b06601
ACS Appl. Mater. Interfaces 2017, 9, 43315−43324

CONCLUSIONS

In summary, physical vapor deposited amorphous Nb_2O_5 integrated on crystallographically oriented Ge offers a new class of oxide/semiconductor heterojunction for wide ranging nanoelectronic applications. To this end, Raman spectroscopic analysis was used to confirm the amorphous nature of as-deposited Nb_2O_5 thin films deposited on epitaxial Ge and bulk Si, which was further corroborated by cross-sectional transmission electron microscopy (X-TEM). High-magnification X-TEM micrographs demonstrated the long- and short-range uniformity of the Nb_2O_5/Ge heterointerface and revealed the formation of an ultrathin GeO_x interlayer, which was attributed to the O_2 ambient utilized during Nb_2O_5 deposition. Variable-angle spectroscopic ellipsometry (VASE) was used to determine the optical band gap of as-deposited Nb_2O_5, indicating a direct gap of 4.3 eV. X-ray photoelectron spectroscopy (XPS) independently validated the VASE-derived band gap via analysis of the O 1s loss spectra from thick (~5 nm) Nb_2O_5 films. Moreover, XPS analysis was used to determine the valence and conduction band offsets (ΔE_V and ΔE_C) at the Nb_2O_5/Ge heterointerface, yielding $\Delta E_V^{(111)} > \Delta E_V^{(110)} > \Delta E_V^{(100)}$ and $\Delta E_C^{(110)} > \Delta E_C^{(100)} > \Delta E_C^{(111)}$ relationships for ΔE_V and ΔE_C, respectively. Ge out-diffusion into the overlying Nb_2O_5 dielectric was observed across all investigated Ge orientations, potentially impacting the measured Nb_2O_5 band gap values due to the formation of the complex Nb_2O_5–GeO_2 composite oxides. Lastly, leveraging the <1.0 eV ΔE_C found for all orientations, metal–insulator–semiconductor (MIS) contacts were fabricated from Nb_2O_5/(100)Ge heterojunctions. A 20× increase in reverse-bias current density was observed via the inclusion of an Nb_2O_5 interlayer between the metal/semiconductor junction, thereby suggesting a reduction in the metal-induced interface gap states at the Ti/n-Ge interface and an improvement in Ohmic behavior across the junction. Consequently, these results provide key guidance for the development of oxide/Ge-based multifunctional devices seeking to leverage the high carrier mobilities of Ge and highly tunable micro- and macroscopic properties of niobium oxides.

MATERIALS AND METHODS

Material Synthesis. The unintentionally doped 80 nm thick Ge epilayers investigated in this work were grown on epi-ready (100)GaAs, (110)GaAs, and (111)A-GaAs substrates utilizing a dual-chamber solid-source molecular beam epitaxy growth process. Two separate growth reactors connected via an ultrahigh vacuum transfer chamber provided in situ growth isolation between III–V and Ge epitaxy. Substrate oxide desorption was performed in the III–V chamber at 680, 580, and 550 °C for the (100)/6°, (110), and (111)A GaAs substrates, respectively, under an As_2 overpressure of ~1×10^{-5} Torr. Reflection high-energy electron diffraction patterns recorded from the sample surface during each growth step were used to provide real-time, in situ growth process feedback. An initial 0.2 μm undoped GaAs homoepitaxial buffer was grown following oxide desorption to generate a smooth surface for subsequent Ge growth. Growth temperatures of 650, 550, and 500 °C were used during GaAs homoepitaxy to maintain an optimized atom surface mobility while minimizing surface species desorption, thereby ensuring planar surface morphologies during growth. Following homoepitaxial GaAs growth, the substrate was transferred to the Ge reactor for Ge epitaxy at a nominal substrate temperature of 400 °C. The low growth temperature employed in this work, coupled with low growth rates of 0.07, 0.078, and 0.1 Å/s for (100)Ge, (110)Ge, and (111)Ge, respectively, aided in the minimization of atomic species diffusion across the Ge/GaAs interface. After Ge epilayer growth, the heterostructures were gradually cooled to prevent thermal-induced stress accumulation and its subsequent relief via defect formation. Complete details of the growth processes are reported elsewhere.[59]

Prior to Nb_2O_5 deposition, the epitaxial Ge/GaAs heterostructures were stripped of native oxides using a 5s $NH_4OH/H_2O_2/H_2O$ (2:1:200) surface treatment. The 2 and 5 nm thick Nb_2O_5 films were then deposited at a deposition rate of ~0.2 Å/s, noting that the target thickness was based on the monitored (nominal) deposition rate. These thicknesses were selected such that (i) the 5 nm Nb_2O_5 will provide a bulklike XPS signal representative of only the oxide and (ii) the 2 nm Nb_2O_5 will provide XPS spectra representative of the oxide/Ge heterointerface. Source material for the Nb_2O_5 deposition utilized commercially available stoichiometric Nb_2O_5 powder (Alfa Aesar, 99.9% purity) uniaxially pressed into pellet targets, with subsequent cold isostatic pressure applied to achieve a high density. The resulting material was then sintered at 1350 °C for 2h to realize a highly dense, high-purity ceramic target suitable for PVD use. An ultrahigh-purity oxygen flow (flow rate ~5 sccm) and room-temperature substrate plate was used throughout the Nb_2O_5 deposition to minimize the formation of substoichiometric niobium oxides.

Materials Characterization. The structural and interface properties of the Nb_2O_5/Ge heterostructures were investigated using cross-sectional transmission electron microscopy (X-TEM) preformed on a JEOL 2100 transmission electron microscope. Conventional mechanical grinding, dimpling, and low-temperature Ar^+-ion milling were used during sample preparation of the cross-sectional electron-transparent foils. The amorphous nature of the as-deposited Nb_2O_5 was further investigated using Raman spectra acquired from a Jobin Yvon Horiba LabRam HR800 system equipped with a 514.32 nm Ar laser excitation source. Independent determination of the Nb_2O_5 band gap was achieved using variable-angle spectroscopic ellipsometry (VASE) and X-ray photoelectron spectroscopy (XPS). Wavelength-dependent ellipsometry spectra (Δ and φ) were measured using a 5 nm increment from 200 to 500 nm.

Additionally, the band alignment at the Nb_2O_5/Ge heterointerface was studied using a PHI Quantera SXM XPS system equipped with a monochromatic Al Kα (E = 1.4867 keV) X-ray source. Pass energy of 26 eV and exit angle of 45° were utilized throughout high-resolution spectral capture. CasaXPS v2.3.14 was then used to fit the measured core level spectra utilizing a Lorentzian peak shape convolved with a Shirley-type background. The full width at half-maximum of each peak was used in determining the precise value for a given core level's binding energy. Further, linear extrapolation of the onset of photoemission at the Fermi edge (with respect to the measurement-dependent background) was used in determining the valence band maximum for each bulklike sample. Uncertainties in the range of 0.05–0.1 eV for ΔE_V and ΔE_C were derived using regression analysis over the linear region of valence emission for each valence band spectrum. As this extrapolation method is sensitive to the data selected during the fitting process, the associated uncertainties are generally dictated by the linearity and stability of photoemission at the Fermi edge, as opposed to the energy resolution. Thus, the uncertainty in the band discontinuities evaluated in this work is predominately due to the precision of the measured spectral features. Additionally, to minimize the effect of positive charge accumulation on the sample surfaces due to photoelectron generation and subsequent electron loss, an in situ electron flood gun was used to provide a continuous flow of electrons and therefore minimize the effects of sample charging on the measured binding energy values.

Lastly, Au/Ti/Nb_2O_5/(100)Ge and Al/Nb_2O_5/(100)Ge metal–insulator–semiconductor (MIS) contacts were fabricated using a negative photolithographic and lift-off process of electron beam-evaporated Au/Ti and Al contact metals. Current–voltage characterization of the fabricated and annealed MIS contacts was performed using a Keithley 4200 SCS semiconductor parametric analyzer and a Cascade Summit 900 probe station equipped with Cascade DCM200 micromanipulators.

DOI: 10.1021/acsami.7b06601
ACS Appl. Mater. Interfaces 2017, 9, 43315–43324

AUTHOR INFORMATION

Corresponding Author

*E-mail: mantu.hudait@vt.edu. Tel: (540) 231-6663. Fax: (540) 231-3362.

ORCID

Mantu K. Hudait: 0000-0002-9789-3081

Michael Clavel: 0000-0002-2925-6099

Notes

The authors declare no competing financial interest.

ACKNOWLEDGMENTS

M.C. and J.-S.L. acknowledge financial support from the National Science Foundation under grant number ECCS-1507950. The authors also acknowledge the Institute for Critical Technology and Applied Science's Nanocharacterization and Fabrication Laboratory, the Virginia Tech Nanofabrication Laboratory, and Charles Farley for assistance in materials characterization.

REFERENCES

(1) Pignolet, A.; Rao, G. M.; Krupanidhi, S. B. Rapid Thermal Processed Thin Films of Niobium Pentoxide (Nb_2O_5) Deposited by Reactive Magnetron Sputtering. *Thin Solid Films* **1995**, *261*, 18−24.

(2) Hadamek, T. Growth of Niobium Oxide Thin Films by Molecular Beam Epitaxy. Master of Arts, University of Texas, 2014.

(3) Gao, W.; Conley, J. F., Jr.; Ono, Y. NbO as Gate Electrode for n-channel Metal-oxide-Semiconductor Field-effect-transistors. *Appl. Phys. Lett.* **2004**, *84*, 4666.

(4) Zhou, Y.; Ramanathan, S. Mott Memory and Neuromorphic Devices. *Proc. IEEE* **2015**, *103*, 1289−1310.

(5) Kim, S.-J.; Cho, B. J.; Yu, M. B.; Li, M.-F.; Xiong, Y.-Z.; Zhu, C.; Chin, A.; Kwong, D.-L. Metal−Insulator−Metal RF Bypass Capacitor Using Niobium Oxide (Nb_2O_5) With HfO_2/Al_2O_3 Barriers. *IEEE Electron Device Lett.* **2005**, *26*, 625−627.

(6) Lee, K.; Kim, J.; Mok, I.-S.; Na, H.; Ko, D.-H.; Sohn, H.; Lee, S.; Sinclair, R. RESET-First Unipolar Resistance Switching Behavior in Annealed Nb_2O_5 Films. *Thin Solid Films* **2014**, *558*, 423−429.

(7) Xu, X.; Tian, B. Z.; Kong, J. L.; Zhang, S.; Liu, B. H.; Zhao, D. Y. Ordered Mesoporous Niobium Oxide Film: A Novel Matrix for Assembling Functional Proteins for Bioelectrochemical Applications. *Adv. Mater.* **2003**, *15*, 1932−1936.

(8) Wang, Z.; Hu, Y.; Wang, W.; Zhang, X.; Wang, B.; Tian, H.; Wang, Y.; Guan, J.; Gu, H. Fast and Highly-sensitive Hydrogen Sensing of Nb_2O_5 Nanowires at Room Temperature. *Int. J. Hydrogen Energy* **2012**, *37*, 4526−4532.

(9) Gimon-Kinsel, M. E.; Balkus, K. J., Jr. Pulsed Laser Deposition of Mesoporous Niobium Oxide Thin Films and Application as Chemical Sensors. *Microporous Mesoporous Mater.* **1999**, *28*, 113−123.

(10) Rho, S.; Jahng, D.; Lim, J. H.; Choi, J.; Chang, J. H.; Lee, S. C.; Kim, K. J. Electrochemical DNA Biosensors Based on Thin gold Films Sputtered on Capacitive Nanoporous Niobium Oxide. *Biosens. Bioelectron.* **2008**, *23*, 852−856.

(11) Rosenfeld, D.; Schmid, P. E.; Széles, S.; Lévy, F.; Demarne, V.; Grisel, A. Electrical Transport Properties of Thin-film Metal-oxide-metal Nb_2O_5 Oxygen Sensors. *Sens. Actuators, B* **1996**, *37*, 83−89.

(12) Nico, C.; Monteiro, T.; Graça, M. P. F. Niobium Oxides and Niobates Physical Properties: Review and Prospects. *Prog. Mater. Sci.* **2016**, *80*, 1−37.

(13) Lira-Cantu, M.; Norrman, K.; Andreasen, J. W.; Krebs, F. C. Oxygen Release and Exchange in Niobium Oxide MEHPPV Hybrid Solar cells. *Chem. Mater.* **2006**, *18*, 5684−5690.

(14) Aegerter, M. A. Sol−gel Niobium Pentoxide: A Promising Material for Electrochromic Coatings, Batteries, Nanocrystalline Solar Cells and Catalysis. *Sol. Energy Mater. Sol. Cells* **2001**, *68*, 401−422.

(15) Varghese, B.; Haur, S. C.; Lim, C.-T. Nb_2O_5 Nanowires as Efficient Electron Field Emitters. *J. Phys. Chem. C* **2008**, *112*, 10008−10012.

(16) Wei, M.; Wei, K.; Ichihara, M.; Zhou, H. Nb_2O_5 Nanobelts: A Lithium Intercalation Host with Large Capacity and High Rate Capability. *Electrochem. Commun.* **2008**, *10*, 980−983.

(17) Fang, X.; Hu, L.; Huo, K.; Gao, B.; Zhao, L.; Liao, M.; Chu, P. K.; Bando, Y.; Golberg, D. New Ultraviolet Photodetector Based on Individual Nb_2O_5 Nanobelts. *Adv. Funct. Mater.* **2011**, *21*, 3907−3915.

(18) Zhao, Y.; Eley, C.; Hu, J.; Foord, J. S.; Ye, L.; He, H.; Tsang, S. C. E. Shape-Dependent Acidity and Photocatalytic Activity of Nb_2O_5 Nanocrystals with an Active TT (001) Surface. *Angew. Chem., Int. Ed.* **2012**, *51*, 3846−3849.

(19) Özer, N.; Chen, D.-G.; Lampert, C. M. Preparation and Properties of Spin-coated Nb_2O_5 Films by the Sol−gel Process for Electrochromic Applications. *Thin Solid Films* **1996**, *277*, 162−168.

(20) Smith, D. L.; Majumdar, S.; Billone, M.; Mattas, R. Performance Limits for Fusion First-Wall Structural Materials. *J. Nucl. Mater.* **2000**, *283−287*, 716−720.

(21) Hadamek, T.; Posadas, A. B.; Dhamdhere, A.; Smith, D. J.; Demkov, A. A. Spectral Identification Scheme for Epitaxially Grown Single-phase Niobium Dioxide. *J. Appl. Phys.* **2016**, *119*, No. 095308.

(22) Aegerter, M. A.; Schmitt, M.; Guo, Y. Sol−gel Niobium Pentoxide Coatings: Applications to Photovoltaic Energy Conversion and Electrochromism. *Int. J. Photoenergy* **2002**, *4*, 1−10.

(23) Liu, H.; Gao, N.; Liao, M.; Fang, X. Hexagonal-like Nb_2O_5 Nanoplates-Based Photodetectors and Photocatalyst with High Performances. *Sci. Rep.* **2015**, *5*, No. 7716.

(24) O'Hara, A.; Nunley, T. N.; Posadas, A. B.; Zollner, S.; Demkov, A. A. Electronic and Optical Properties of NbO_2. *J. Appl. Phys.* **2014**, *116*, No. 213705.

(25) Pan, L.; Wang, Y.; Wang, X.; Qu, H.; Zhao, J.; Li, Y.; Gavrilyuk, A. Hydrogen Photochromism in Nb_2O_5 Powders. *Phys. Chem. Chem. Phys.* **2014**, *16*, 20828−20833.

(26) Song, J.; Han, C.; Lai, P. T. Comparative Study of Nb_2O_5, NbLaO, and La_2O_3 as Gate Dielectric of InGaZnO Thin-Film Transistor. *IEEE Trans. Electron Devices* **2016**, *63*, 1928−1933.

(27) O'Hara, A.; Demkov, A. A. Nature of the Metal−insulator Transition in NbO_2. *Phys. Rev. B* **2015**, *91*, No. 094305.

(28) Usha, N.; Sivakumar, R.; Sanjeeviraja, C.; Arivanandhan, M. Niobium Pentoxide (Nb_2O_5) Thin Films: rf Power and Substrate Temperature Induced Changes in Physical Properties. *Optik* **2015**, *126*, 1945−1950.

(29) de Filho, D. A. B.; Franco, D. W.; Filho, P. P. A.; Alves, O. L. Niobia Films: Surface Morphology, Surface Analysis, Photoelectrochemical Properties and Crystallization Process. *J. Mater. Sci.* **1998**, *33*, 2607−2616.

(30) Özer, N.; Rubin, M. D.; Lampert, C. M. Optical and Electrochemical Characteristics of Niobium Oxide Films Prepared by Sol-gel Process and Magnetron Sputtering: A Comparison. *Sol. Energy Mater. Sol. Cells* **1996**, *40*, 285−296.

(31) Tanabe, K. Catalytic Application of Niobium Compounds. *Catal. Today* **2003**, *78*, 65−77.

(32) Ramírez, G.; Rodil, S. E.; Muhl, S.; Turcio-Ortega, D.; Olaya, J. J.; Rivera, M.; Camps, E.; Escobar-Alarcón, L. Amorphous Niobium Oxide Thin Films. *J. Non-Cryst. Solids* **2010**, *356*, 2714−2721.

(33) Kukli, K.; Ritala, M.; Leskelä, M. Development of Dielectric Properties of Niobium Oxide, Tantalum Oxide, and Aluminum Oxide Based Nanolayered Materials. *J. Electrochem. Soc.* **2001**, *148*, F35−F41.

(34) Kukli, K.; Ritala, M.; Leskelä, M.; Sajavaara, T.; Keininen, J.; Gilmer, D. C.; Hegde, R.; Rai, R.; Prabhu, L. Atomic Layer Deposition of HfO_2 Thin Films and Nanolayered $HfO_2−Al_2O_3−Nb_2O_5$ Dielectrics. *J. Mater. Sci.: Mater. Electron.* **2003**, *14*, 361−367.

(35) Yoshimura, K.; Miki, T.; Iwama, S.; Tanemura, S. Characterization of Niobium Oxide Electrochromic Thin Films Prepared by Reactive d.c. Magnetron Sputtering. *Thin Solid Films* **1996**, *281−282*, 235−238.

(36) Hunsche, B.; Vergöhl, M.; Neuhäuser, H.; Klose, F.; Szyszka, B.; Matthée, T. Effect of Deposition Parameters on Optical and

DOI: 10.1021/acsami.7b06601
ACS Appl. Mater. Interfaces 2017, 9, 43315−43324

Mechanical Properties of MF- and DC-sputtered Nb_2O_5 Films. *Thin Solid Films* **2001**, *392*, 184−190.
(37) Lai, F.; Lin, L.; Huang, Z.; Gai, R.; Qu, Y. Effect of Thickness on the Structure, Morphology and Optical Properties of Sputter Deposited Nb_2O_5 Films. *Appl. Surf. Sci.* **2006**, *253*, 1801−1805.
(38) Foroughi-Abari, A.; Cadien, K. C. Growth, Structure and Properties of Sputtered Niobium Oxide Thin Films. *Thin Solid Films* **2011**, *519*, 3068−3073.
(39) Serényi, M.; Lohner, T.; Petrik, T.; Zolnai, Z.; Horváth, Z. E.; Khánh, N. Q. Characterization of Sputtered and Annealed Niobium Oxide Films using Spectroscopic Ellipsometry, Rutherford Backscattering Spectrometry and X-ray Diffraction. *Thin Solid Films* **2008**, *516*, 8096−8100.
(40) Venkataraj, S.; Drease, R.; Liesch, Ch.; Kappertz, O.; Jayavel, R.; Wuttig, M. Temperature Stability of Sputtered Niobium-oxide Films. *J. Appl. Phys.* **2002**, *91*, 4863.
(41) Leskelä, M.; Ritala, M. Atomic Layer Deposition (ALD): From Precursors to Thin Film Structures. *Thin Solid Films* **2002**, *409*, 138−146.
(42) Kukli, K.; Ritala, M.; Leskelä, M.; Lappalainen, R. Niobium Oxide Thin Films Grown by Atomic Layer Epitaxy. *Chem. Vap. Deposition* **1998**, *4*, 29−34.
(43) Hara, N.; Takahashi, T.; Yoon, J. H.; Sugimoto, K. Ellipsometric Analysis of Growth Process and Corrosion Resistance of Nb_2O_5 Films Formed by MOCVD. *J. Electrochem. Soc.* **1994**, *141*, 1669−1674.
(44) Agarwal, G.; Reddy, G. B. Study of Surface Morphology and Optical Properties of Nb_2O_5 Thin Films with Annealing. *J. Mater. Sci.: Mater. Electron.* **2005**, *16*, 21−24.
(45) Graça, M. P. F.; Saraiva, M.; Freire, F. N. A.; Valente, M. A.; Costa, L. C. Electrical Analysis of Niobium Oxide Thin Films. *Thin Solid Films* **2015**, *585*, 95−99.
(46) Strømme, M.; Niklasson, G. A.; Ritala, M.; Leskelä, M.; Kukli, K. $(Ta_{1-x}Nb_x)_2O_5$ films Produced by Atomic Layer Deposition: Temperature Dependent Dielectric Spectroscopy and Room-temperature I−V Characteristics. *J. Appl. Phys.* **2001**, *90*, 4532.
(47) Masse, J.-P.; Szymanowski, H.; Zabeida, O.; Amassian, A.; Klemberg-Sapieha, J. E.; Martinu, L. Stability and Effect of Annealing on the Optical Properties of Plasma-Deposited Ta_2O_5 and Nb_2O_5 Films. *Thin Solid Films* **2006**, *515*, 1674−1682.
(48) McConnell, A. A.; Aderson, J. S.; Rao, C. N. R. Raman Spectra of Niobium Oxides. *Spectrochim. Acta, Part A* **1976**, *32*, 1067−1076.
(49) Balachandran, U.; Eror, N. G. Raman Spectrum of the High Temperature Form of Nb_2O_5. *J. Mater. Sci. Lett.* **1982**, *1*, 374−376.
(50) Khorasaninejad, M.; Walia, J.; Saini, S. S. Enhanced First-order Raman Scattering from Arrays of Vertical Silicon Nanowires. *Nanotechnology* **2012**, *23*, No. 275706.
(51) Iatsunskyi, I.; Jurga, S.; Smyntyna, V.; Pavlenko, M.; Myndrul, V.; Zaleska, A. Raman Spectroscopy of Nanostructured Silicon Fabricated by Metal-assisted Chemical Etching. *Proc. SPIE* **2014**, *9132*, No. 913217.
(52) Hudait, M. K.; Zhu, Y.; Jain, N.; Maurya, D.; Zhou, Y.; Varghese, R.; Priya, S. $BaTiO_3$ Integration with Nanostructured Epitaxial (100), (110), and (111) Germanium for Multifunctional Devices. *ACS Appl. Mater. Interfaces* **2013**, *5*, 11446−11452.
(53) Hudait, M. K.; Clavel, M.; Zhu, Y.; Goley, P.; Kundu, S.; Maurya, D.; Priya, S. Integration of $SrTiO_3$ on Crystallographically Oriented Epitaxial Germanium for Low-power Device Applications. *ACS Appl. Mater. Interfaces* **2015**, *7*, 5471−5479.
(54) ltokawa, H.; Maruyama, T.; Miyazaki, S.; Hirose, M. In *Determination of Bandgap and Energy Band Alignment for High-Dielectric-Constant Gate Insulators Using High-Resolution X-ray Photoelectron Spectroscopy*, Extended Abstracts of the 1999 International Conference on Solid State Devices and Materials, Tokyo, 1999; pp 158−159.
(55) Miyazaki, S. Photoemission Study of Energy-band Alignments and Gap-state Density Distributions for High-k gate Dielectrics. *J. Vac. Sci. Technol., B: Nanotechnol. Microelectron.: Mater., Process., Meas., Phenom.* **2001**, *19*, 2212.
(56) Miyazaki, S. Characterization of High-k Gate Dielectric/silicon Interfaces. *Appl. Surf. Sci.* **2002**, *190*, 66.
(57) Zhang, W. F.; Nishimula, T.; Nagashio, K.; Kita, K.; Toriumi, A. Conduction Band Offset at GeO_2/Ge Interface Determined by Internal Photoemission and Charge-corrected X-ray Photoelectron Spectroscopies. *Appl. Phys. Lett.* **2013**, *102*, No. 102106.
(58) Kraut, E. A.; Grant, R. W.; Waldrop, J. R.; Kowalczyk, S. P. Semiconductor Core-Level to Valence-Band Maximum Binding-Energy Differences: Precise Determination by X-ray Photoelectron Spectroscopy. *Phys. Rev. B* **1983**, *28*, 1965−1977.
(59) Hudait, M. K.; Zhu, Y.; Jain, N.; Hunter, J. L., Jr. Structural, Morphological, and Band Alignment Properties of GaAs/Ge/GaAs Heterostructures on (100), (110) and (111)A GaAs Substrates. *J. Vac. Sci. Technol., B: Nanotechnol. Microelectron.: Mater., Process., Meas., Phenom.* **2013**, *31*, No. 011206.
(60) Brillson, L. J. *Surfaces and Interfaces of Electronic Materials*; Wiley-VCH: Weinheim, Germany, 2010.
(61) Perego, M.; Seguini, G. Charging Phenomena in Dielectric/Semiconductor Heterostructures during X-ray Photoelectron Spectroscopy Measurements. *J. Appl. Phys.* **2011**, *110*, No. 053711.
(62) Perego, M.; Molle, A.; Seguini, G. Electronic Properties at the Oxide Interface with Silicon and Germanium through X-ray Induced Oxide Charging. *Appl. Phys. Lett.* **2012**, *101*, No. 211606.
(63) Manik, P. P.; Lodha, S. Contacts on n-type Germanium using Variably Doped Zinc Oxide and Highly Doped Indium Tin Oxide Interfacial Layers. *Appl. Phys. Express* **2015**, *8*, No. 051302.
(64) Lin, J.-Y. J.; Roy, A. M.; Nainani, A.; Sun, Y.; Saraswat, K. C. Increase in Current Density for Metal Contacts to n-Germanium by Inserting TiO_2 Interfacial layer to Reduce Schottky Barrier Height. *Appl. Phys. Lett.* **2011**, *98*, No. 092113.

DOI: 10.1021/acsami.7b06601
ACS Appl. Mater. Interfaces 2017, 9, 43315−43324